## *Invited Paper*
# Image Processing of Thermal Infrared Images

*John R. Schott*
Rochester Institute of Technology, Center for Imaging Science, One Lomb Memorial Drive, Rochester, NY 14623

ABSTRACT: Techniques for digital processing of thermal infrared images are addressed. In particular, techniques that are uniquely required for thermal imagery are emphasized. This includes a treatment of how to implement absolute temperature calibration algorithms, methods for registering and combining multiple thermal infrared images, and methods for combining thermal infrared reflected visible and near-infrared data. In addition the characteristics and methods for analysis of apparent thermal inertia images and thermal infrared multispectral images are treated.

## INTRODUCTION

THIS PAPER REVIEWS a variety of image processing techniques used for thermal infrared (TIR) image analysis. The emphasis is on how image processing techniques are used to solve problems unique to TIR imagery. While many of the techniques discussed may also be used for analysis of conventional electro-optical (EO) images, TIR imaging often has unique problems or analysis requirements which will be emphasized here. Those aspects of TIR image processing which are common to conventional EO image analysis will generally not be treated. The processing of TIR imagery is typically driven by a need to extract information about the temperature of Earth surface features or some thermodynamically related variable (e.g., rate of change of temperature or thermal inertia). This interest in extraction of temperature information has led to an emphasis on image processing techniques capable of yielding quantitative radiometric solutions on a pixel-by-pixel basis. These point processing techniques are typically implemented with some form of look-up table (LUT). The peculiarities of TIR LUTs, including their essential non-linearities, are discussed in the section on point processing.

While TIR image geometry is essentially identical to similar EO systems, many airborne TIR systems have applications which require geometric corrections which are often not required of their EO counterparts. Thus, certain image processing methods for geometric correction of airborne scanner imagery are discussed.

Many applications of TIR imagery require use of ancillary data derived from maps or other images. The processing of these data pose several problems unique to TIR imagery, including registration of images with poor brightness correlation and processing of pixels differentially on the basis of the optical properties of the material imaged (e.g, emissivity effects). Several image processing techniques for using multiple images to solve absolute temperature measurement problems are discussed, including parallel processing approaches where applicable. Many investigators have suggested that use of multiple TIR images can provide information on important cultural, geological, and agricultural variables. Techniques for combining multi-temporal and multispectral TIR imagery for resource assessment are achieving growing acceptance. The use of these image combination techniques and ways to display multiple image sets for TIR image information extraction are presented in some detail.

## BACKGROUND

TIR imagers typically operate in the midwave (3 to 5µm) or long-wave (8 to 14µm) infrared region. Table 1 contains a comparison of selected features of several TIR imagers. Most quan-

TABLE 1.

| Imaging System | Spectral Response [µm] | IFOV [mR] or Ground Spot Size [km] | Noise Level [K] | Data Quantization [bits] |
|---|---|---|---|---|
| Landsat Thematic Mapper (Band 6) (TM) | 10.4-12.4 | 0.12 km | 0.4K | 8 |
| Heat Capacity Mapping Radiometer (HCMM) | 10.5-12.5 | 0.83 mR | 0.4K | 8 |
| Advanced Very High Resolution Radiometer (AVHRA) | 3.55-3.93 10.3-11.3 11.5-12.5 | 1.51 mR 1.41 mR 1.30 mR | 0.12K | 10 |
| Thermal Infrared Multispectral Scanner (TIMS) | 8.2-8.6 8.6-9.0 9.0-9.4 9.4-10.2 10.2-11.2 | 2.5 mR | 0.1-0.3K | 8 |

titative work utilizes the long-wave IR region or the midwave IR at night to avoid solar reflection effects that make quantitative analysis of daytime data in the midwave extremely difficult. In general, daytime midwave effects will not be included here. With this condition, the effective spectral radiance observed by an airborne or space-based TIR sensor system can be expressed in simplified form as (*cf.* Figure 1)

$$L_\lambda = \epsilon_T L_{T\lambda} \tau_\lambda + r_\lambda L_{d\lambda} \tau_\lambda + L_{u\lambda} \qquad (1)$$

where

$L_\lambda$ is the observed spectral radiance [$\text{wm}^{-2}\text{sr}^{-1}\mu\text{m}^{-1}$],
$\epsilon_\lambda$ is the wavelength dependent emissivity,
$L_{T\lambda}$ is the spectral radiance from a blackbody at temperature $T$ according to the Planck blackbody equation,
$\tau_\lambda$ is the wavelength dependent atmospheric transmission,
$L_{d\lambda}$ is the spectral downwelled radiance onto the target due to self-emission by the sky,
$r_\lambda$ is the wavelength dependent reflectivity,
$L_{\mu\lambda}$ is the spectral upwelled radiance due to self-emission from the atmosphere between the target and the sensor, and
$\lambda$ is wavelength.

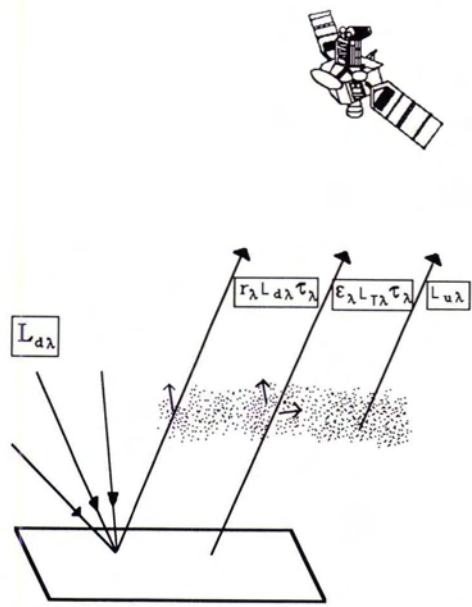The sensors are typically line scanners or whisk broom scan-

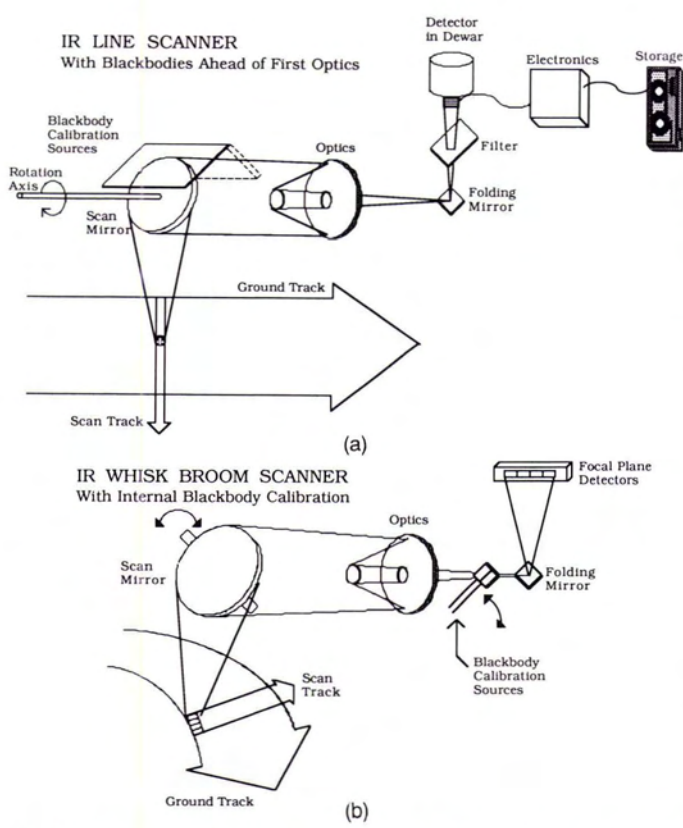FIG. 1. Spectral radiance reaching a remote sensing platform.



FIG. 2. Typical optical diagrams for(a) an airborne TIR Line Scanner with full aperture blackbodies ahead of the collecting mirror and (b) a satellite TIR whisk broom scanner with an internal blackbody calibrator.
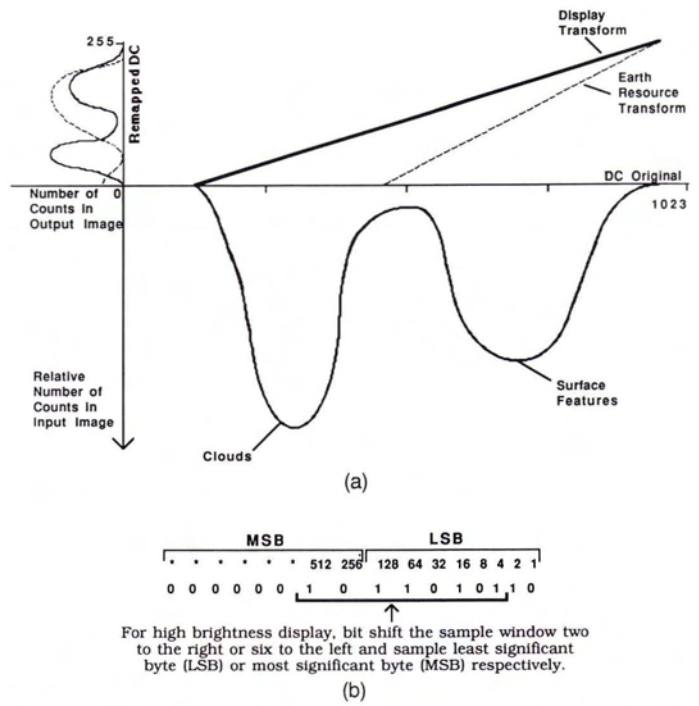


FIG. 3. Look-up tables can be used for initial ten-bit to eight-bit remapping for image display or image processing of selected features based on (a) histogram analysis. Alternately, (b) the high or low eight bits can be easily sampled.

because of their relatively small apertures (75 to 125 mm), use full field-of-view temperature controlled blackbodies located ahead of the first optical surface for calibration. These blackbodies are viewed by the scan mirror during the "dead" time when it looks upward into the scanner housing. The larger aperture of most satellite systems makes this approach to calibration impractical. As illustrated in Figure 2b, blackbody calibration surfaces are introduced into the optical train much closer to the detectors where their physical size can be greatly reduced. This is the approach taken with band 6 of the Landsat Thematic Mapper where calibration radiance sources are briefly introduced into the field-of-view of the optics during the scan mirror turnaround time.

Most TIR sensor systems are designed such that the recorded signal is linearly related to the observed radiance such that

$$\text{DC} = m\left[\int_x^x L_\lambda \beta_\lambda d\lambda\right] + b$$
$$= mL + b \tag{2}$$

where

DC is the recorded signal level (digital count for a digital system),

$\beta_\lambda$ is the normalized spectral response function of the sensor,

$m$ is the system gain term incorporating optical throughput and electronic amplification,

$L$ is the effective radiance observed by the sensor [wm$^{-2}$sr$^{-1}$], and

$b$ is the system bias incorporating radiometric and electronic offset terms.

Thus, only two reference levels are needed for internal calibration of the sensor's response. In the next section, image

ners, as illustrated in Figure 2, with either full aperture calibration or internal calibration. Generally, airborne line scanners,

processing procedures for implementing internal sensor calibrations will be discussed.

It is often useful to express TIR radiance levels in terms of the more intuitively meaningful units of apparent temperature. This refers to the temperature a blackbody would have to be at to produce the radiance level in question in the bandpass of interest. This concept can be extended to introduce the concept of noise equivalent temperature difference (NEΔT) as the change in the temperature of a blackbody needed to produce a change in radiant power at the detector equal to the noise equivalent power (NEP) of the system (i.e., just at the detection limit). These temperature equivalences are common in TIR image processing and will be utilized in the following sections.

## POINT PROCESSING

Point processing (the independent processing of each pixel's brightness regardless of the brightness of neighboring pixels) is used for radiometric calibration of TIR images. For individuals used to processing images with one byte or less per pixel (i.e., 256 or fewer gray levels), many TIR images may be a surprise. To accommodate the wide thermal range of Earth surface features (e.g., tropical deserts to high clouds) while maintaining high thermal resolution (i.e., NEΔT values of tenths of a degree K) many sensors have more than 8 bit quantizers. For serial processing using high levels of integer precision or floating point operations, this should present no problem. However, many image processing and/or display systems are hardware limited to handling 8-bit images. This often requires an initial brightness remapping of images for display purposes and a subsequent (usually different) remapping for processing purposes if the full radiometric resolution is to be maintained. Figure 3 shows how two such remapping look-up tables might be generated from an initial 10-bit histogram. In many systems it may be simpler and yield acceptable first-look results to sample the low eight bits (e.g., if only clouds were of interest in the sample shown) or the high eight bits (e.g., if only Earth surface features are of interest), of the 10 bits used. In general, this requires bit shifting algorithms to shift the data of interest to the most significant or least significant byte of a two byte data set which can then be sampled for further processing. (cf. Figure 3b).

Radiometric calibration of TIR imagery begins with the sampling of the digital records of the calibration sources. For many systems, each line of data includes the signal from the Earth scan as well as short scans over two calibration sources (blackbodies) of known radiance. The digital count corresponding to the signal level from the calibration sources must be sampled for each line. The radiance from each source is computed from telemetry or flight data recording the temperature of the blackbodies. These data coupled with the spectral response data for the sensor permit a unique solution to Equation 2 for each line of data. Depending on the noise characteristics of the sensor, these calibrations will then be applied on a line-by-line basis, averaged over several lines or included in a many line smoothing solution which generates modified line-by-line corrections. For systems with calibration sources after the forward optics, additional corrections for attenuation and self-radiance from these optics must be made to the $m$ and $b$ terms of Equation 2. These are typically precalibrated adjustments to the calibration described above with slight corrections required if the temperature of the large optical elements changes or if deterioration of the optical coatings occurs. In general, all the corrections are first-order linear so the functional form of Equation 2 remains stable (i.e., the corrections are adjustments to the observed $m$ and $b$ values). In many cases (e.g., TM band 6 P tapes) the data are pre-processed to remove line-by-line variations so the calibration constants ($m$ and $b$) are fixed for the entire image.

As indicated in Figure 1, the radiance reaching the sensor is modified by atmospheric effects such that the radiance computed by internal sensor calibration must be further corrected to obtain estimates of the radiance leaving the ground. Often, Equation 1 can be simplified to

$$L = \tau L(0) + L_u \qquad (3)$$

where $L$ is the radiance observed by the sensor,

$\tau$ is the effective atmospheric transmission in the bandpass (these terms include corrections for the spectral shape of the source and the spectral response of the sensor),

$L(0) = \epsilon L_T + rL_d$ is the effective ground-leaving radiance in the bandpass,

$\epsilon$ is the emissivity in the bandpass,

$L_T$ is the effective blackbody radiance in the bandpass from a sample at temperature $T$,

$L_d$ is the effective downwelled radiance in the bandpass,

$r = 1 - \epsilon$ is the reflectivity in the bandpass, and

$L_u$ is the effective upwelled radiance in the bandpass.

The terms $\tau$ and $L_u$ are dependent on the atmospheric conditions at the time of data acqisition. A number of techniques exist for computing these values to varying degrees of accuracy (cf. Byrnes and Schott, 1986). One of the most common methods involves use of radiation propagation models such as LOWTRAN 6 (Kneizy et al., 1983) which can be used to generate estimates of $\tau$, $L_u$, and $L_d$.

In order to convert surface leaving radiance $L(0)$ values to apparent surface temperature values, the Planck blackbody ra-
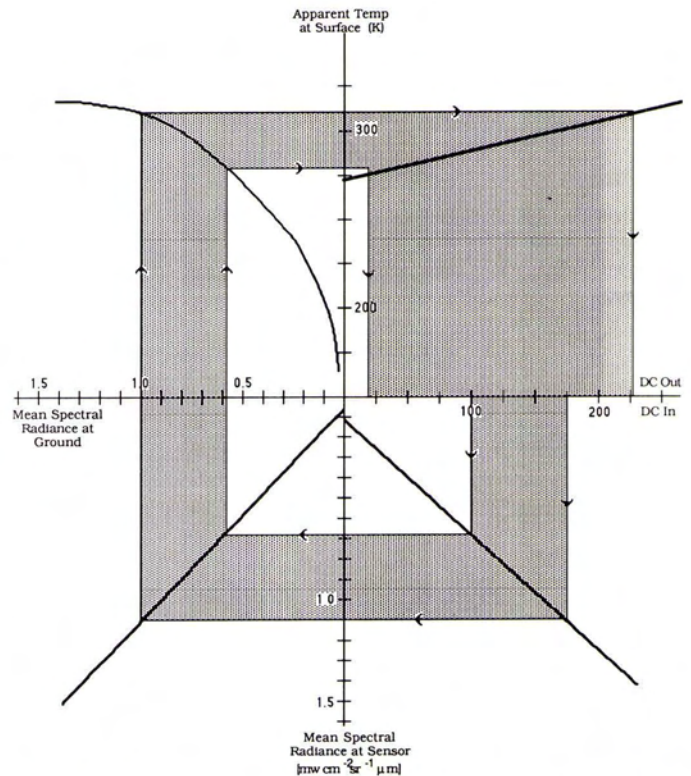


FIG. 4. Graphs of look-up tables used in converting input digital counts to output digital counts directly related to apparent surface temperature. The shaded area indicates how the range of digital counts in the input image would be mapped to output digital counts.

| | Nominal line start<br>for level platform | | | | | | | | | | | |
|---|---|---|---|---|---|---|---|---|---|---|---|---|
| | Zero Fill | | | | | | | | | | | |
| Level —✈— Line 1 | 0 | 0 | 0 | 0 | 0 | 27 | 38 | 50 | 53 | 90 | 120 | ••• |
| Roll a —✈— Line 2 | 0 | 0 | 24 | 25 | 27 | 28 | 37 | 51 | 60 | 92 | 118 | ••• |
| Roll b —✈— Line 3 | 0 | 0 | 0 | 0 | 0 | 0 | 0 | 0 | 0 | 0 | 119 | ••• |

a) Roll = f(gyro) = -8 milliradians ≅ -3 IFOV's
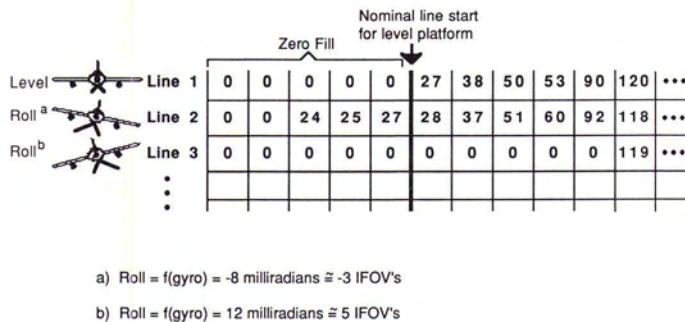
b) Roll = f(gyro) = 12 milliradians ≅ 5 IFOV's

FIG. 5. Illustration of how the start of line is advanced or delayed from the vertical start location for roll in a 2.5-milliradian IFOV system. Note: integer number of pixels are shown here for simplicity (i.e., nearest neighbor resampling), other types of resampling (e.g., bilinear or cubic convolution) could be used.

diation equation can be solved by numerical methods to yield a relationship between effective surface leaving radiance observed in the bandpass and the blackbody equivalent temperature. The relationship between $L(0)$ and temperature is monotonic, non-linear, and bandpass dependent. NASA (1984) expresses the relationship between temperature and radiance in the Landsat 5 TM band 6 bandpass as

$$T = \frac{K_2}{\ln\left[\dfrac{K_1}{L_\lambda} + 1\right]} \tag{4}$$

where $K_1 = 60.776$ mw cm$^{-2}$ sr$^{-1}$ μm$^{-1}$ and $K_2 = 1260.56$ $K$.

Whole image implementation of these calibration techniques yield images whose digital counts are simple linear functions of apparent surface temperature. The image processing techniques employ cascaded look-up tables (LUTs) which can be implemented serially but are more commonly implemented in parallel using image processing display devices employing addressable LUTs. Individual LUTs are shown conceptually in Figure 4 for clarity. The bottom right quadrant of Figure 4 represents the relationship between recorded digital count and radiance at the sensor (or in this case mean spectral radiance at the sensor) as in Equation 2. The bottom left quadrant represents the relationship between mean spectral radiance at the sensor and surface-leaving spectral radiance as in Equation 33. The upper left quadrant represents the relationship between spectral radiance in the bandpass and temperature from Equation 4. Finally, the upper right quadrant is a convenient linear remapping from apparent temperature to digital count to fill the dynamic range of an 8-bit system. In practice, the LUTs shown graphically in Figure 4 would be cascaded together, and only a single look-up table operation would be performed to reduce quantization errors. An important feature to note in Figure 4 is that, although the transfer curves are drawn as continuous, the input and output images are discrete (i.e., quantized) and, therefore, the entire process is discrete. Because the initial quantization is essentially done in radiance space and the output is in temperature space, the input digital count steps do not correspond to equal temperature steps across the dynamic range of the final image. The output images from this process are useful for many purposes but still contain emissivity effects which mask true (kinetic) temperature variations. Before considering methods for processing TIR images to kinetic temperature maps, it is important to consider the geometric integrity of the image.

## GEOMETRIC CORRECTIONS AND CONTOUR MAPPING

Baseline geometric correction for TIR sensors is essentially identical to any other EO sensor (cf. Schowengerdt, 1983) and
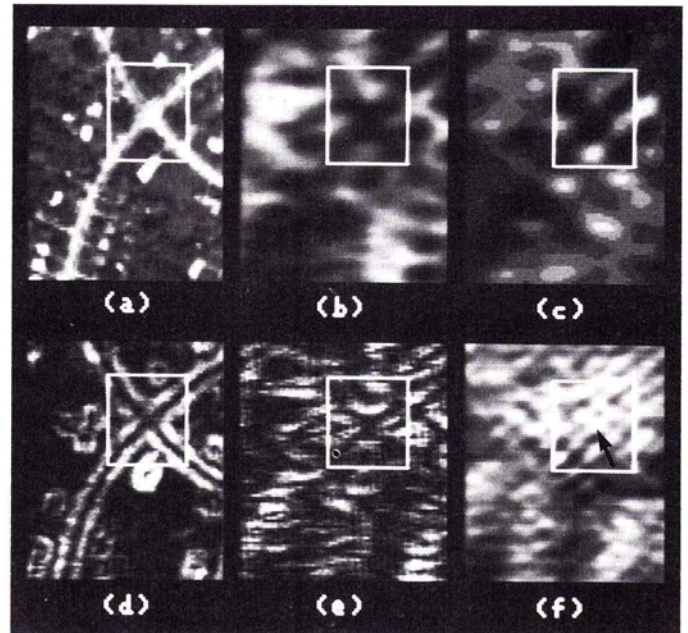


FIG. 6. Example of the use of correlation for automatic control point selection. (a) is a reflected visible image, (b) is a TIR (8- to 14-μm) image of the same area (these images are approximately 85 pixels by 85 pixels at 2 m/pixel). (c) is the correlation of the search window shown in (a) with (b) where the correlation at each point is proportional to the brightness (the search window is shown in (b) for reference), (d) and (e) are the gradient images of (a) and (b), respectively, and (f) is the correlation of the search window in (d) with (e). Note that the brightness in (c) has been greatly enhanced so that the low correlation values can be observed. The peak correlation value in (c) is a low value and at the incorrect location, whereas the peak correlation value in (f) is high and correctly located in the center of the window as highlighted by the arrow.
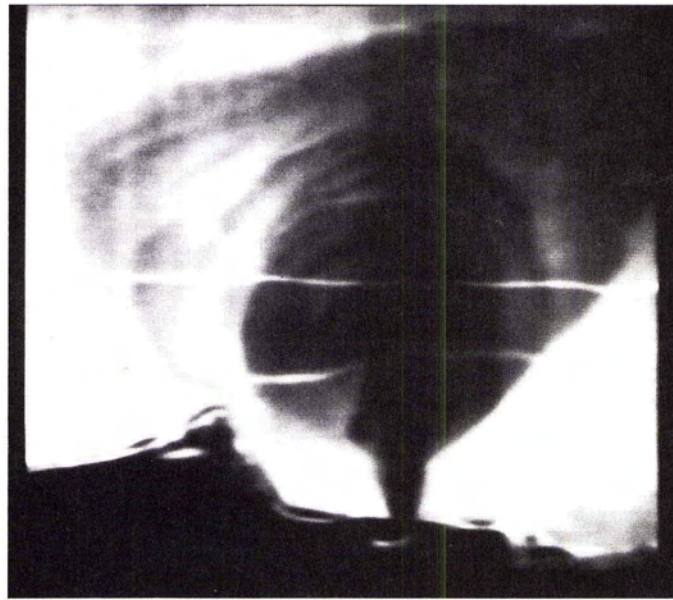
will not be treated here for satellite sensors. However, airborne scanner TIR images must often be geometrically corrected where their EO counterparts are often not. This is because mapping quality imagery is generally more readily obtained from aerial photos than from EO scanners. Because thermal maps must be generated from aerial TIR systems, airborne scanner geometric correction will be briefly treated, with the treatment being equally applicable at any wavelength. Geometric distortion in airborne systems can come from any number of sources, but the most common are associated with aircraft orientation (roll, pitch, and yaw) and aircraft velocity ($v$) to altitude ($h$) mismatch relative to scan speed (referred to as $v/h$ distortion). Of these systematic effects, pitch and yaw are generally small, fairly constant, and easily removed to first order by subsequent registration steps. The $v/h$ errors result in compression or stretch in the along-track direction resulting from successive scan lines not projecting to the ground in exactly unit instantaneous field-of-view increments. For geometrically correct images to occur, the following equation must hold:

$$\frac{v}{h} \quad R \cdot \text{IFOV} \tag{5}$$

where

$v$    is aircraft ground speed [m/sec],

$h$    is aircraft altitude (AGL) [m],

$R$    is the collection mirror scan rate [revolutions/sec], and

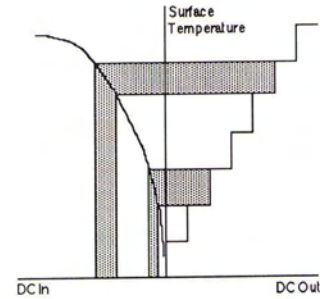IFOV  is the instantaneous field of view [radians].

The parameters on the right-hand side of Equation 4 are often constants, and aircraft or mission requirements limit control of the left-hand side variables, resulting in systematically distorted
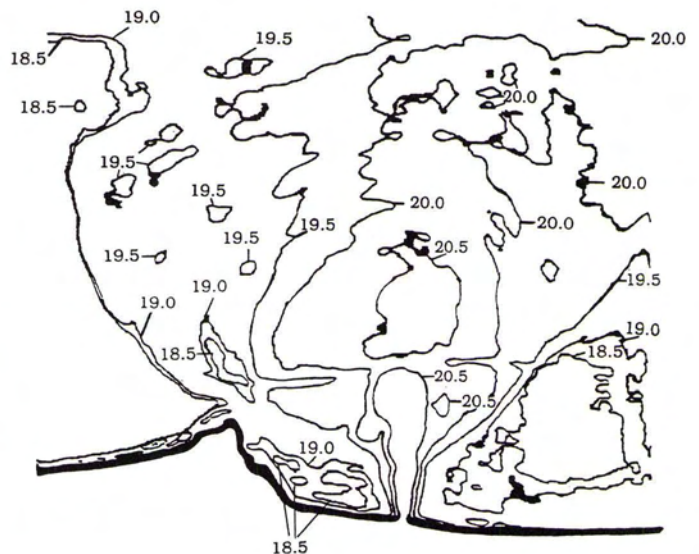
FIG. 7. Steps followed in generation of an isothermal surface temperature map from a TIR image. (a) is a geometrically and radiometrically corrected radiance image of a power plant cooling water discharge (black-hot), (b) is an LUT used to generate gray level steps at fixed surface temperature increments (note how different brightness ranges in the input image map to equal temperature steps in the final image), (c) is the image that results from passing (a) through the process illustrated in (b) and (d) is the final isothermal map shown at the same scale as the images.

imagery. However, to the extent that the velocity ($v$) and altitude ($h$) parameter are known, simple first-order corrections can be applied to stretch or compress the $x$ axis. Velocity variations within an image compound this problem significantly and require piecewise solutions. Roll errors are always present in airborne scanner data. While pilots can generally restrict the variability in pitch and yaw, differential roll within an image, and even line-to-line, must be expected. In some systems, this is overcome by mounting the scanner on a gyroscopically stabilized platform within the aircraft. Servos controlled by the gyroscope keep the scanner platform parallel with the plane of the Earth while the aircraft, in effect, rolls about the platform. This approach requires a sizeable investment in equipment and space (not only for the additional equipment but also to allow for motion of the scanner within the aircraft). An alternative

method of roll compensation involving image processing is often employed. In this case, a gyroscope signal proportional to the amount of roll is recorded along with each line of imagery. When the image is geometrically corrected, each line is preceded by zero fill prior to the start of the line. The amount of roll is computed from the gyroscope signal and divided by the IFOV of the system. The resulting value defines how many pixels to advance or delay the start of each line relative to the nominal line start location within the zero fill (cf. Figure 5).

The first-order geometric corrections described thus far are suitable for generation of an image without severe visual geometric distortions. Conventional scaling and rotation methods would permit the generation of an image in nominally the same format as a map or another image of the same area. The TIR image could then be registered to the map or image using man-
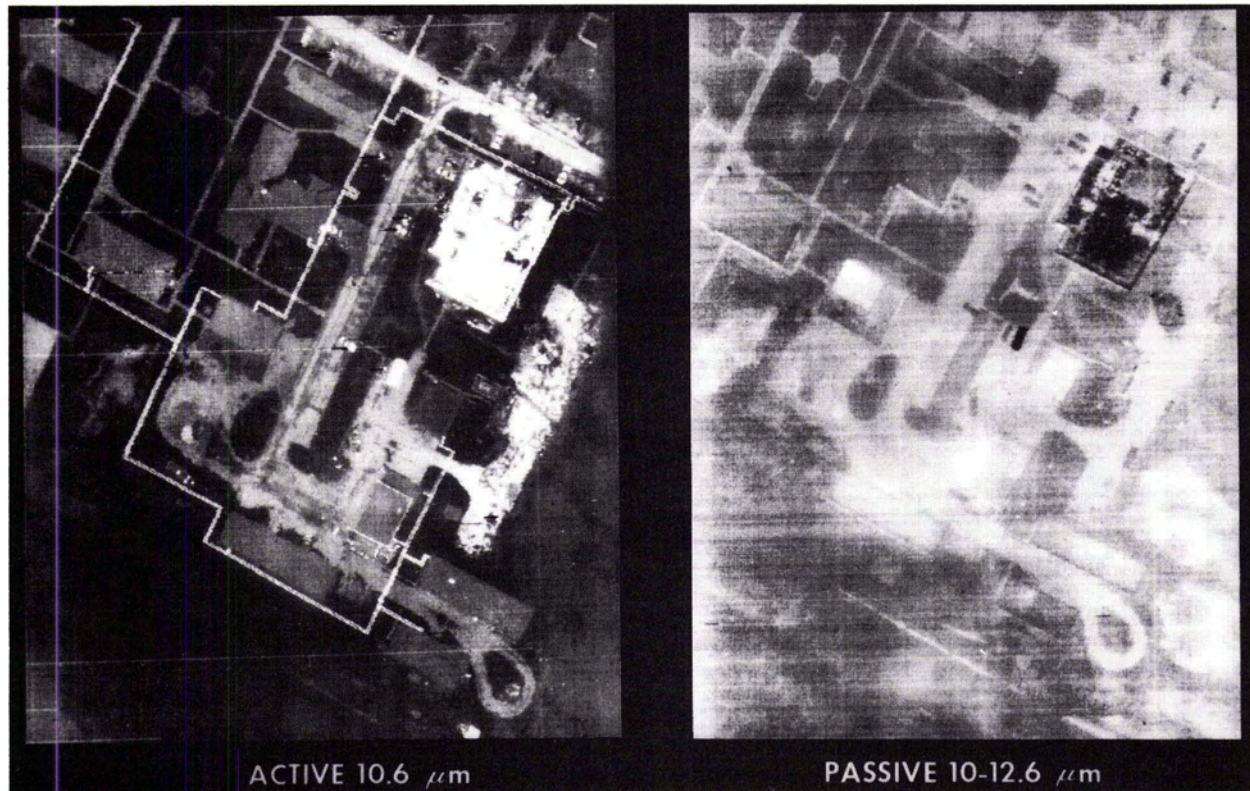
FIG. 8. Active and passive imagery acquired in the LWIR spectral region. (a) Active image acquired with a 10.6-$\mu$m $CO_2$ image. (b) Passive TIR image acquired in the 10- to 10.6-$\mu$m region. (Imagery courtesy of Don Lowe, ERIM.)

ually selected control points and resampling techniques. Image-to-image registration (TIR to TIR and TIR to reflected visible or infrared) is highly desirable for TIR image analysis, and automated control point selection would greatly facilitate this process. Schowengerdt (1983) describes how images that have been geometrically corrected to first order (e.g., $v/h$, roll, scale, and rotation for a TIR image) and resampled can be registered to similar images using correlation techniques for automated control point selection. However, automated registration of TIR images with other images using conventional brightness correlation methods is generally not possible. This is due to the lack of consistent brightness correlation between self-emitted images acquired at different times of the day or between TIR images and visible or near infrared images. It is possible to overcome this limitation by using correlation techniques on edge information derived from each image (e.g., gradient images). The gradient image, $G$, can be defined (cf. Gonzalez and Wintz, 1987) as

$$G(x,y) = |I(x,y)vI(x+1,y)| + |I(x,y) - I(x,y+1)| \quad (6)$$

where $I$ is the original image brightness value and $x$ and $y$ define pixel coordinates. An example of this approach is shown in Figure 6.

One of the motivations for geometric correction of TIR images is to facilitate the generation of isothermal maps. Isothermal maps are often used to monitor power plant cooling water discharges where permit regulations are often expressed in terms of surface areas which cannot be raised more than some number of degrees above ambient. It is important, therefore, that both the image geometry and radiometry be correct. Contour (isothermal) mapping is performed by passing a geometrically and radiometrically corrected image (cf. Figure 7a) through a stepped look-up table as illustrated in Figure 7b. The brightness steps in the image (cf. Figure 7c) are then mapped either manually or

using edge-following algorithms to generate final isothermal maps as illustrated in Figure 7d. The thermal image shown in Figures 7a and 7c is shown with brightness decreasing with increasing radiance; thus, the hot water plume is black. The horizontal white line through the center of the image shows the aircraft ground track and is removed in the final map making. The lower white line through the plume is a boat wake whose cooling impact is preserved in the final map.

## PROCESSING OF MULTIPLE IMAGES

Radiometric calibration using the radiation propagation modeling approach described earlier (e.g., LOWTAN) is often limited by incomplete knowledge of atmospheric conditions. To overcome this limitation, numerous "in-scene" techniques have been developed to attempt to reduce the need for ancillary data (cf. Schott, 1979; Chedin et al., 1982; Prabhakara et al., 1974). One of these approaches utilizes multiple spectral bands within the same atmospheric window such as the to 11.3-$\mu$m and the 11.5- to 12.5-$\mu$m bands of the NOAA AVHRR sensor. The theory described in detail by Prabhakara et al. (1974) and McMillan (1975) is based on the differential extinction in the two bands. Under conditions when the assumptions associated with the technique hold (clear atmospheres, equal apparent radiometric temperatures for the atmosphere in the two bands, significantly different extinction cross section, and modest temperature ranges) the surface temperature on a pixel-by-pixel basis can be expressed as

$$T(O) - \frac{T_1 - RT_2}{1 - R} \quad (7)$$

where

$T(O)$ is the apparent temperature [K] associated with the surface leaving radiance $L(O)$,

(a)

AIRCRAFT THERMAL INERTIA (JULY 13, 1977)



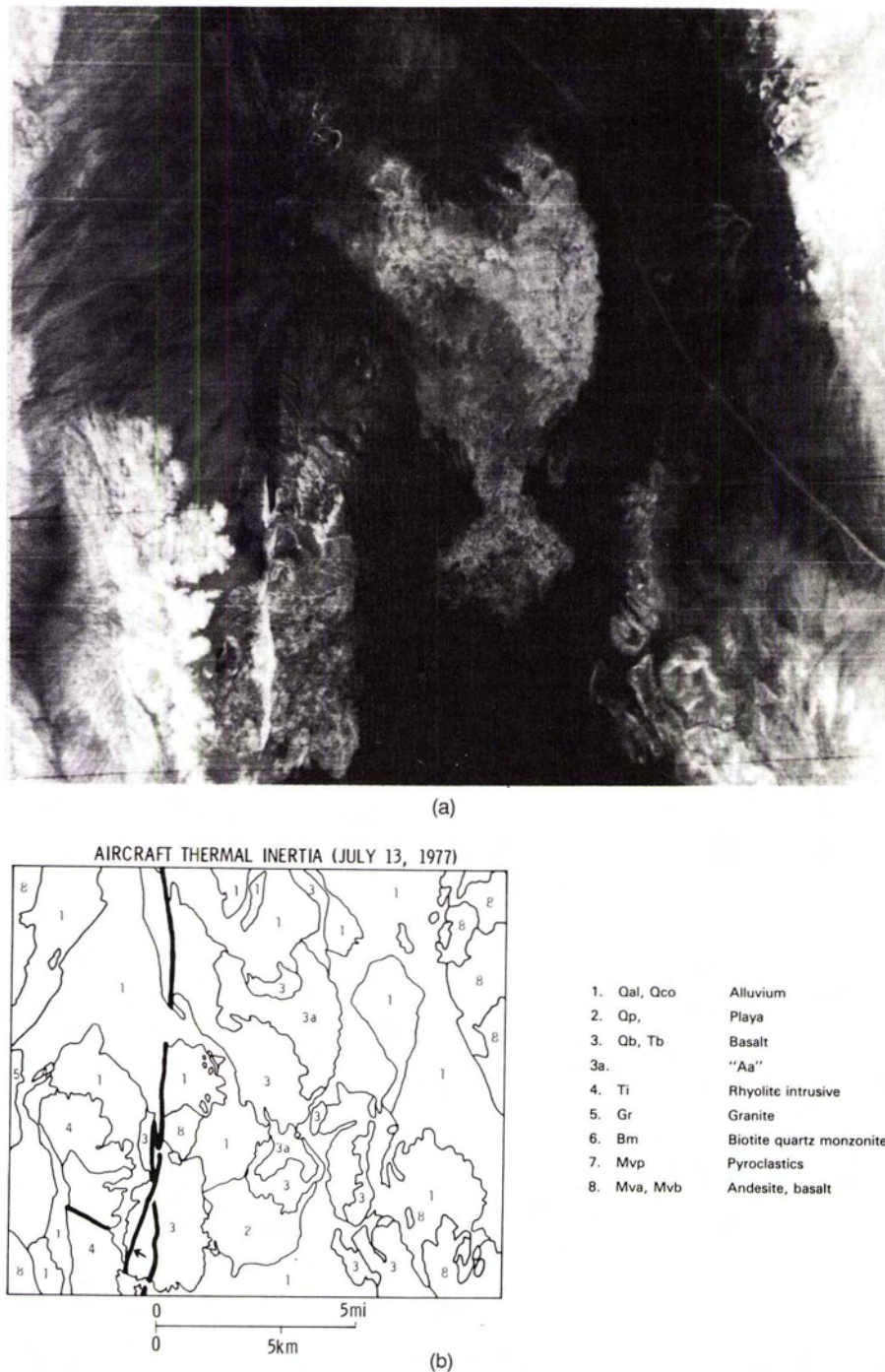| 1. | Qal, Qco | Alluvium |
|---|---|---|
| 2. | Qp, | Playa |
| 3. | Qb, Tb | Basalt |
| 3a. | | "Aa" |
| 4. | Ti | Rhyolite intrusive |
| 5. | Gr | Granite |
| 6. | Bm | Biotite quartz monzonite |
| 7. | Mvp | Pyroclastics |
| 8. | Mva, Mvb | Andesite, basalt |

0          5mi

0      5km

(b)

FIG. 9. (a) Thermal-inertia image of Pisgah Crater and surroundings made from 1977 aircraft scanner data. Image covers 18-by 20-km area (from Kahle, 1982); (b) sketch map of interpreted distribution of geologic units at Pisgah Crater. Note separation of "aa" lava from main basalt flow. (From kahle, 1982) [reproduced from Short and Stuart, 1982]

$T_1$ and $T_2$ are the apparent temperatures [K] observed by the sensor in band 1 and band 2 respectively, and

$R$ is the ratio of the extinction cross sections in band 1 to the extinction cross-section in band 2.

Using the point processing techniques described earlier, apparent temperature images ($T_1$ and $T_2$) can be generated for each of the two registered bands. This involves the steps shown in Figure 4 with step 4b omitted. Equation 7 can then be easily implemented serially or in parallel because it only involves multiplication by constants and simple image differences. In cases where image noise is significant, modified versions of this technique can be employed on large regions of uniform temperature where pixel averaging will reduce noise and improve estimates of $T_1$ and $T_2$. After solving for the ground leaving radiance (from $T(O)$ values) for several areas of different radiance, Equation 3
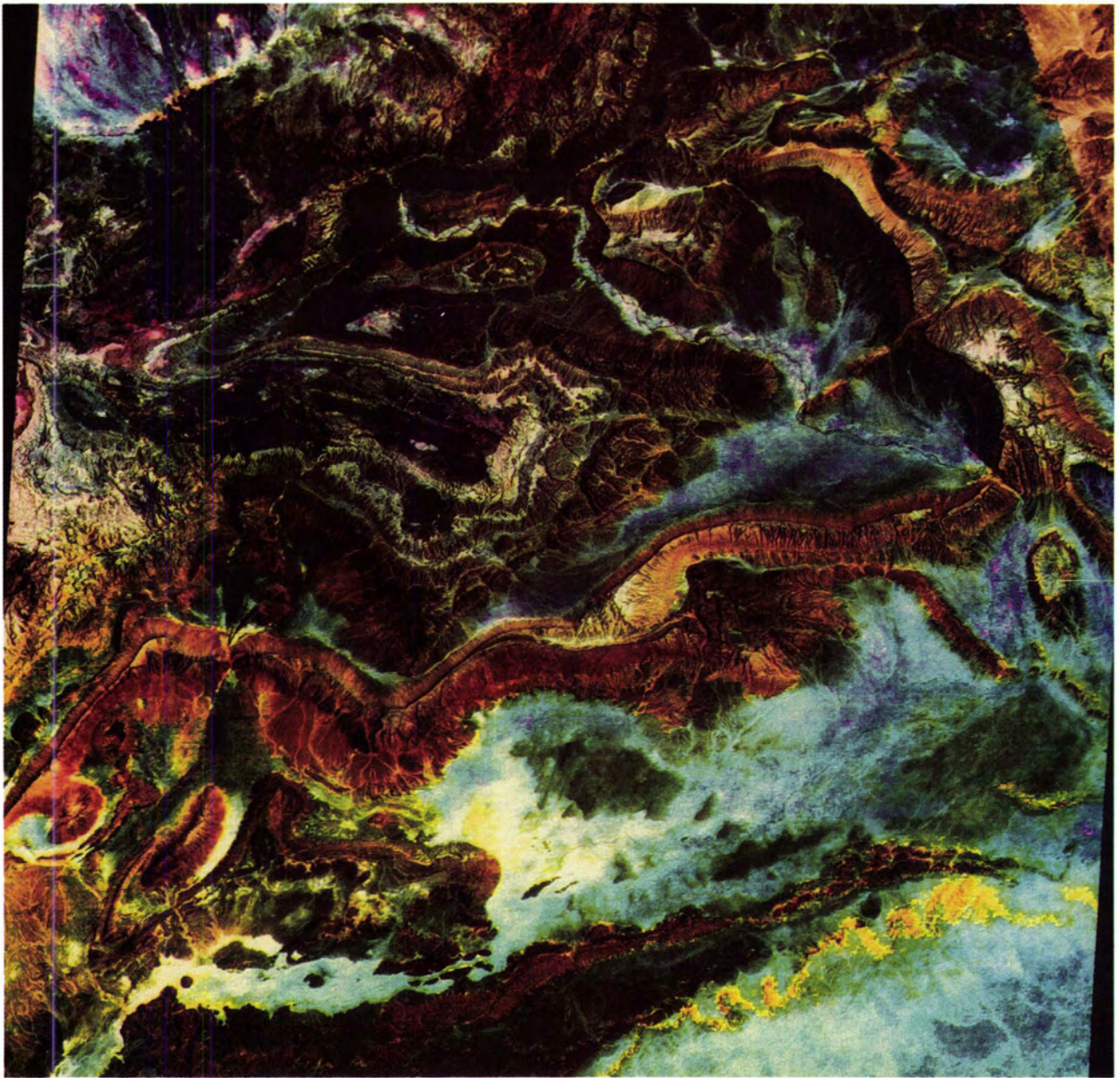
PLATE 1. IHS display of combined Landsat MSS data and HCMM TIR data. The MSS image is displayed as intensity, HCMM night IR is hue and HCMM and IR is saturation. (The scene of Morocco was produced by Haydn (1982) and was reproduced from Short and Stuart (1982).)

can be solved for either band by regression and the LUT approach described earlier can be used on that band to generate apparent surface temperature images.

In many cases the radiometric, or apparent temperature, images described to this point are inadequate and true or kinetic temperature images are required. This requires the generation of an emissivity map in geometric registration with the imaged area. Depending on the scale of the imagery, this map might be generated from land-cover maps, engineering drawings, or some other ancillary source of material type. The emissivity map would be generated by assigning tabulated emissivity values to each material in the map. In many cases the following approximation is used. First, a surface leaving radiance image is generated using the LUT approach described above. Then, if

the downwelled radiance is assumed small and/or the emissivities quite high, the following assumption can be made:

$$L(O) = \epsilon L_T + r L_d \cong \epsilon L_T \tag{8}$$

The blackbody equivalent surface radiance can, therefore, be obtained by dividing the emissivity map (image) into the surface radiance image. The resulting blackbody radiance ($L_T$) image can then be transformed into a kinetic temperature image using the LUT techniques described previously. More accurate results can be obtained if $L_d$ values are known by multiplying a reflectivity map ($r = 1 - \epsilon$) by the downwelled radiance value, subtracting the resulting image from the surface leaving radiance
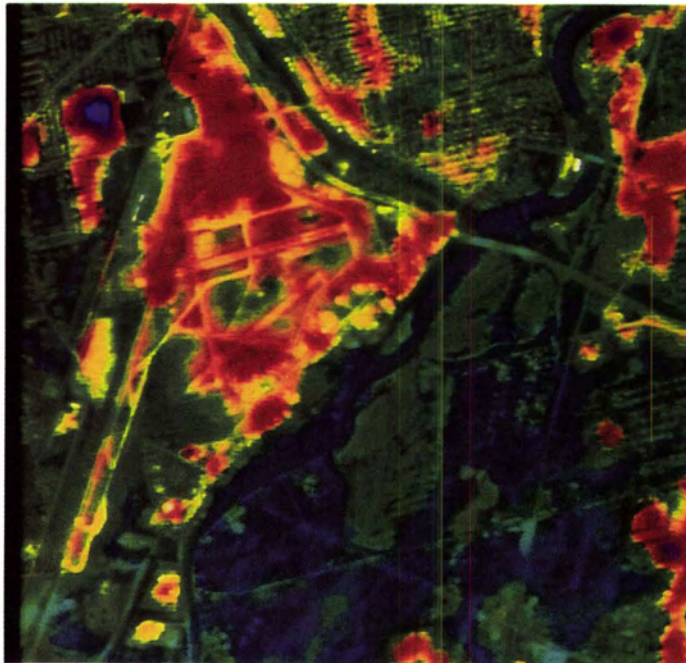
(a)
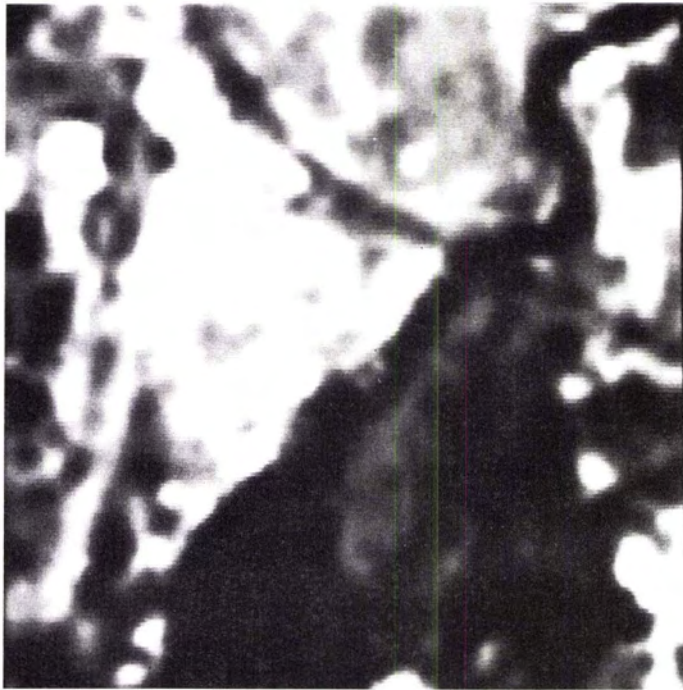


(b)

PLATE 2. (a) IHS temperature image of Rochester, New York, with hue proportional to kinetic temperature derived from Landsat TM and intensity proportional to SPOT panchromatic brightness. Blue is cold with green through red indicating increasing temperature. (b) is an enhanced version of the TM TIR image used to generate (a). Note the dramatic increase in the thermal and spatial interpretability of (a). The airport and residential street patterns are clearly visible.

image and then dividing by the emissivity map (*cf.* Salvaggio and Schott, 1988); i.e.,

$$L_T = \frac{L(O) - rL_d}{\epsilon}. \qquad (9)$$

Several methods have been suggested for generation of the emissivity maps. Salvaggio and Schott (1988) used multispectral classification of TM data to generate land-cover maps. Each land cover was then assigned an emissivity, creating an emissivity map, and the TM thermal channel was analyzed using the procedure described above to generate a kinetic temperature image. Lowe (1978) proposed an alternative approach using simultaneously acquired active and passive imagery in the LWIR region. In the active case a 10.6-μm $CO_2$ laser is used with an airborne line scanner to illuminate the area scanned generating a reflected image. Simultaneously, a conventional TIR image is acquired in the 10 to 12.6 μm bandpass by a second aerial line scanner (*cf.* Figure 8). If the emissivity (reflectivity) is assumed constant over the bandpass, then the brightness in the active image is proportional to the reflectivity and can be calibrated (in Lowe's case, using ground truth) to generate an emissivity and/or reflectivity map. Once the passive and active images are registered, the analytical approach described above can be used to generate kinetic temperature images. This approach has the distinct advantage of directly accounting for emissivity variations both between and within material classes. Lowe points out, however, that spectral variation in emissivity values is not uncommon and caution must be taken in using a narrow band (10.6-μm) reflectivity as indicative of a bandpass (10- to 12.6-μm) value. In particular, strong differential absorption is common for road and building materials due to quartz reststrahlen in the LWIR region.

Day-night radiance or temperature difference images have been used by several investigators as a means of studying material properties that are associated with differential thermal properties. Moore (1982), for example, suggested that the amount of water present in surface soils should influence the day-night temperature difference, with moist soils showing smaller changes due to their higher heat capacity. Also, the high latent heat of evaporation tends to keep moist soils cool during the daytime. The Heat Capacity Mapping Mission (HCMM) sensor was designed to study just this type of problem with TIR data collected approximately 12 hours apart near the extremes of the diurnal heating and cooling cycle. Registered day-night TIR images from the HCMM sensor could be differenced and the image data correlated with field soil moisture studies. Moore reports strong correlation between HCMM derived data and soil moisture but stresses the need for additional corrections associated with crop canopy coverage.

Other HCMM users have employed a term called the apparent thermal inertia (ATI) to study important thermal properties of materials (*cf.* HCMM User's Guide). The ATI value is defined as

$$\text{ATI} = \text{NC}(1-a)/\Delta T \qquad (10)$$

where
    NC is a scale factor,
    $a$  is the surface albedo, and
    $\Delta T$ is the day-night temperature difference.
Under certain circumstances, ATI is highly correlated with the actual thermal inertia which measures a material's resistance to changes in temperature when subjected to thermal loads. The thermal inertia (TI) is defined as

$$\text{TI} = \sqrt{kpc} \qquad (11)$$

where
    $k$ is the thermal conductivity,
    $r$ is the density, and
    $c$ is the specific heat.

Thus, according to Equation 10, highly absorbing objects (low albedo) exhibiting small day-night temperature differences would
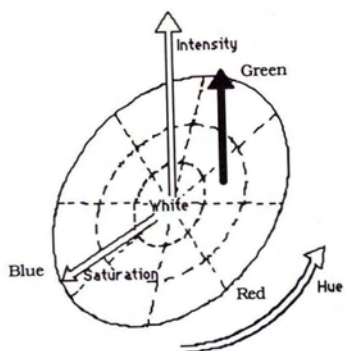
FIG. 10. Illustration of the intensity, hue, and saturation (IHS) color space. The vector shown would be pastel yellow (red-green) of medium brightness.

have the highest ATI values, indicating that little temperature change occurred even though thermal loading levels were very high. Thermal inertia varies significantly for various rock types (*cf.* Reeves, 1975), and ATI measurements have been most extensively used in geologic studies (*cf.* Kahle, 1982; Watson, 1982). In fact, Price (1985) points out that ATI is only correlated with TI under restricted circumstances such as the dry exposed areas often of interest for geologic studies.

Kahle (1982) generated ATI images by first calibrating HCMM day-night registered TIR images to surface temperature using atmospheric propagation models. The surface albedo values were generated from daytime HCMM images acquired in the 0.56- to 1.04-μm spectral band. The brightness in this visible-near infrared (VIS-NIR) band is proportional to albedo, and the proportionality constant can be estimated (ignoring atmospheric effects) from data supplied in the *HCMM Users Guide*. The resulting registered albedo and temperature images can be processed serially or in parallel using Equation 10 to yield an ATI image, i.e., an image whose brightness is proportional to ATI. Kahle (*cf.* Figure 9) indicates that brightness variations in the resultant images can contribute substantially to the mapping of significant geological units.

Improvements in detector technology have led the way to new sensors capable of acquiring multispectral TIR data (i.e., TIR images in many narrow spectral bands, often within the same atmospheric window). Kahle and Goetz (1983) describe the thermal infrared multispectral scanner (TIMS) and its utility in studying geologic features (*cf.* Table 1). In earlier work Kahle *et al*. (1980) had reported on techniques for processing multispectral LWIR imagery. They indicated that the various spectral bands in the 8- to 14-μm atmospheric window were all highly correlated because the image brightness in each band was predominately a function of temperature, as described by Equation 1. In order to generate decorrelated data, a principal components analysis was performed (*cf.* Schowengerdt, 1983). The first principal component image was very highly correlated with temperature but the remaining principal component images were highly decorrelated with temperature. In fact, Kahle *et al*. (1980) suggest that variations in these higher order principal component images are largely a function of emissivity variations driven by material type changes in the image. Thus, principle component image processing techniques or variations suggested by Kahle *et al*. (1980) can be used to extract additional information about geologic structure. In this instance, the TIR multispectral data are being processed to remove thermal effects so that spectral variations in emissivity indicative of different rock types can be more clearly studied.

## DISPLAY OF TIR IMAGES

Most users will be familiar with isothermal mapping, and color coding by brightness (temperature) level to display TIR images. However, in addition to these conventional techniques, numerous exotic methods have been developed to display TIR data with the goal of providing more information to the user in an interpretable manner. Kahle (1982) used an approach involving HCMM TIR day-night and VIS-NIR images displayed simultaneously using the red, green, and blue channels of a color display. In all cases, the compliment or brightness inverse values (i.e., bright maps to dark and vice versa) were used with VIS-NIR data driving the green channel, day-IR the blue channel, and night-IR the red channel. Kahle indicates that the resulting display can be useful to help delineate rock formations, but cautions that unique separation of geologic features is often not possible by this approach alone. Haydn (1982) utilized the intensity hue and saturation (IHS) color space to display the same information. The IHS space is intended to be more directly aimed at visually perceived dimensions than conventional RGB color space (*cf.* Conrac Corporation, 1985). In the IHS color space illustrated in Figure 10, intensity corresponds to visually perceived brightness, hue to the dominant color or wavelength, and saturation to the purity of the color (i.e., unsaturated colors move towards pastels and eventually white). Haydn displayed registered HCMM VIS-NIR as intensity, HCMM night IR as hue, and HCMM day IR as saturation. He found that the resulting displays were useful in helping to delineate geological formations. By registering higher resolution Landsat MSS data (80m/ pixel) to the HCMM TIR data (600m/pixel) and replacing the HCMM VIS-NIR image with the Landsat image in the IHS display, much higher apparent spatial detail was achieved, yielding more interpretable results. Indeed, the resulting displays carried all the same thermal data but had dramatically improved spatial detail. (*cf.* Plate 1).

Salvaggio and Schott (1988) have also used the IHS color space to display TIR data. In this case, a kinetic temperature image was generated using the point processing methods described above, including corrections for emissivity effects and reflected downwelled radiance (*cf.* Equation 9). The surface radiance image $L(O)$ was generated for 120-m pixels by analysis of the TIR band of the Landsat TM using LOWTRAN derived values for $\tau$ and $L_u$. This image was pixel replicated to generate 16 pixels on 30-metre centers for each 120-m pixel. The VIS-NIR channels of the TM were used to generate a land-cover map using supervised gaussian maximum likelihood techniques. Each land-cover type was then assigned an emissivity value resulting in a 30m/ pixel emissivity image. This image was combined with the surface radiance image, and a downwelled radiance value ($L_d$) was obtained from LOWTRAN to yield a blackbody radiance image $L_t$ at simulated spot size of 30m/pixel. The blackbody radiance image was corrected to a kinetic temperature image using the steps illustrated in Figure 4. A SPOT 10 m panchromatic image was registered with the TM scene. The data were then displayed using the IHS color space with the SPOT 10-m data as intensity, the temperature image as hue, and the saturation fixed at maximum. The resultant images are more readily interpreted due to the improved spatial detail and clearly interpretable thermal patterns (*cf.* Plate 2).

## SUMMARY

Numerous image processing techniques have been utilized to process TIR images. The point processing techniques described here have been extensively used to radiometrically correct TIR images to temperature space. When these point processing methods are coupled with geometric correction techniques, they can be used to generate spatially and radiometrically accurate isothermal maps. In addition to the cooling water

temperature mapping applications presented here, isothermal mapping has also been used to study a variety of phenomena where temperature patterns are important. Schott and Schimminger (1982) used this approach to map the thermal bar pattern in the Great Lakes. Schott and Schimminger (1982) and Carlson (1982) also employed this approach to study the urban heat island phenomena.

The rapidly expanding capabilities of computers and parallel image processing systems has led to a significant increase in the use of techniques involving multiple images for analysis of TIR images. The techniques described here for enhanced radiometric calibration, analysis, and display have become practical due to the increased speed and flexibility of image processing systems. As these capabilities continue to expand more and more, TIR image processing is likely to involve analysis of multiple image and multiple sensor data sets. These image processing techniques should allow more detailed spatial and radiometric assessment of thermodynamic phenomena and a better understanding of thermally driven earth resource phenomena.

## REFERENCES

Byrnes, Arthur E., and John R. Schott, 1986. Correction of thermal imagery for atmospheric effects using aircraft measurement and atmospheric modeling techniques, *Applied Optics*, Vol. 25, No. 15, pp. 2563–2570.

Carlson, T. N., 1982. *Applications of HCMM Satellite Data to the Study of Urban Heating Patterns*, NTIS #82N21685.

Chedin, N., N. A. Scott, and A. Berroir, 1982. A single channel, double-viewing angle method for sea surface temperature determination from coincident METEOSAT and TIRO-N radiometric measurements, *J. of Applied Meterology Society*, Vol. 21, pp. 613–618.

Conrac Corporation, 1985. *Raster Graphics Handbook*, 2nd edition, VonNostran Reinhold Company, New York.

Gonzalez, R. L., and P. Wintz, 1987. *Digital Image Processing*, 2nd edition, Addison-Wesley, Reading, Mass.

Haydn, R., 1982. *Multidisciplinary Investigations on HCMM Data Over Middle Europe and Morocco. . .Southern Germany, and Marrakech, Morocco*, NTIS #82N24588.

Kahle, A. B., 1982. *Geologic Application of Thermal Inertia Imaging Using HCMM Data. . .Walker Lake, Nevada: San Rafael, Utah; Death Valley and Pisgah Crater, Lavic Lake Region, California*, NTIS #82N25590.

Kahle, A. B., and Alexander F. H. Goetz, 1983. Mineralogic information from a new airborne thermal infrared multispectral scanner," *Science*, Vol. 222, No. 4619, pp. 24–27.

Kahle, A. B., D. P. Madura, and J. M. Soha, 1980. Middle infrared multispectral aircraft scanner data: analysis for geological applications, *Applied Optics*, Vol. 19, No. 14, pp. 2279–2290.

Kidwell, K. B. (ed.), 1986. *NOAA Polar Orbiter Data Users Guide*, NOAA/NESDIS National Climatic Data Center Satellite Data Services Division, Washington, D. C.

Kneizys, F. X., E. P. Shettle, W. O. Gallery, J. H. Chetwynd, Jr., L. W. Abrev, J. E. A. Selby, S. A. Clough, and R. W. Fenn, 1983. *Atmospheric Transmittance/Radiance Computer Code LOWTRAN 6*, Air Force Geophysics Laboratory, Optical Physics Division. 1983

Lowe, Donald S., 1978. Effects of emissivity on airborne observation of roof temperature, *Proceedings of thermosense 1*, sponsored by The American Society of Photogrammetry.

McMillan, L. M., 1975. Estimation of sea surface temperatures from two infrared window measurements with different absorptions, *J. Geophysical Research*, Vol. 80, pp. 5113–5117.

Moore, D. G., 1982. *Evaluation of HCMM Data for Assessing Soil Moisture and Water Table Depths*, NTIS #82N22600. 1982

NASA, 1978. *Heat Capacity Mapping Mission (HCMM) Data Users Handbook for Applications Explorer Mission-A (AEM)*, (revised) Prepared by the Goddard Space Flight Center, National Aeronautics and Space Administration.

———, , 1984. *Thematic Mapper Design Through Flight Evaluation*, Final Report (revised) Santa Barbara Research Center, Report 41741, NASA Contract NAS5-24200.

Prabhakara, C., G. Dalu, and V. G. Kunde, 1974. Estimation of sea surface temperature from remote sensing in the 11 to 13 µm window region, *J. Geophysical Research*, Vol. 79, No. 33.

Price, J. C., 1985. On the analysis of thermal infrared imagery: the limited utility of apparent thermal inertia, *Remote Sensing of Environment*, Vol. 18, pp. 59–77. 1985

Reeves, Robert G. (ed.) 1975. *Manual of Remote Sensing*, American Society of Photogrammetry, Falls Church, Virginia, Vol. 1, p. 83.

Salvaggio, Carl, and John R. Schott, 1988. "Enhanced display of thermal infrared image data using HIS coding," Presented at Electronic Imaging East '88, International Imaging Exposition and Conference, Boston, Mass.

Schott, J. R., 1979. Temperature measurement of cooling water discharged from power plants, *Photogrammetric Engineering and Remote Sensing*, Vol. 45, No. 6, pp. 753–761.

Schott, J. R., and E. Schimminger, 1981 *Data Use Investigations for Applications Explorer Mission A (Heat Capacity Mapping Mission)*, Calspan Report No. 6175-M-1, NASA NTIS #E81-10079.

Schowengerdt, Robert A., 1983. *Techniques for Image Processing and Classification in Remote Sensing*, Academic Press, New York, N.Y.

Short, Nicholas MN., and Locke M. Stuart, Jr., 1982. *The Heat Capacity Mapping Mission (HCMM) Anthology*, National Aeronautics and Space Administration.

Watson, K., 1982. *Application of HCMM Data to Regional Geologic Analysis for Mineral and Energy Resource Evaluation*, NTIS #84N16625, 1982